

Numerical modeling of evaporator surface temperature of a micro loop heat pipe at steady-state condition

M Ghajar and J Darabi

Department of Mechanical Engineering, MEMS and Microsystems Laboratory,
University of South Carolina, Columbia SC 29208, USA

E-mail: darabi@engr.sc.edu

Received 6 April 2005, in final form 30 June 2005

Published 6 September 2005

Online at stacks.iop.org/JMM/15/1963

Abstract

Numerical investigations have been performed to simulate a novel micro loop heat pipe (MLHP) under steady-state conditions. For most electronics, the maximum working temperature is an important design factor; therefore an accurate prediction of this temperature is crucial. The model predicts the steady-state temperature distribution at the surface of the heat source as a function of applied heat loads. This code builds upon a previous code developed by the authors (Ghajar *et al* 2005 *J. Micromech. Microeng.* **15** 313–21), and utilizes a hybridizing of an alternating direction implicit (ADI) computational fluid dynamics (CFD) code and relevant thermodynamic equations. Using this simulation tool, the minimum required compensation chamber cavity has been calculated and checked for various operating temperature ranges. Additionally, the design of the MLHP has been improved by evaluating the effects of the geometric feature variations. Considering the fabrication constraints, some of the optimized geometry dimensions were found to be a groove wall thickness of 2 μm , a groove width of 7 μm , a wicking structure length of 500 μm and a vapor line width of 2 mm.

(Some figures in this article are in colour only in the electronic version)

Nomenclature

A	area	ξ	coordinate fitted in the direction of the liquid line
α	liquid fraction of the CC (hot base)	L	length
α^*	grooves aspect ratio	ρ	density (kg m^{-3})
β	liquid fraction of the CC (cold base)	σ	surface tension (N m^{-1})
CC	compensation chamber	T	temperature ($^{\circ}\text{C}$)
CLS	capillary limit solving	W	width
C	specific heat capacity ($\text{kJ kg}^{-1} \text{K}^{-1}$)	Subscripts	
D	depth	1	evaporator exit condition
f	friction factor	2	condenser entrance
ΔP	pressure drop (Pa)	3	start of subcooling in condenser
ΔT	Temperature difference ($^{\circ}\text{C}$)	4	condenser exit
∇	gradient operator	5	grooves' condition at liquid line-end
h	convective heat transfer coefficient ($\text{W m}^{-2} \text{K}^{-1}$)	appl	applied
k	Thermal conductivity ($\text{W m}^{-1} \text{K}^{-1}$)	cap	capillary
KH	Kaya–Hoang's or Hoang–Kaya's method [11, 12]	CC	compensation chamber
		con	condenser

e	evaporator
Ext	external
g	grooves
h	hydraulic
l	liquid
ll	liquid line
sat	saturation
sink	sink
sc	subcooled
surf	outside wall of the evaporator
tot	total
v	vapor, vapor line
w	wick, wall

Introduction

The importance of electronics cooling continues to remain substantial due to ever-improving microelectronics technologies and the consequent elevated power consumption density. Loop heat pipes, derived from heat pipes, have proven efficient for space and ground spot-cooling applications where high heat fluxes suppress the possibility of applying conventional cooling systems. A number of experimental and numerical modeling efforts have been made over the past several decades following the invention of the loop heat pipe by Gerasimov and Maidanik [2]. A brief history and literature study has been included in a previous publication of the authors [1] and other researchers [3–9] and is therefore not repeated here for the purpose of brevity. A complete review of loop heat pipe studies can be found in [10].

Basically, there are two distinct approaches adopted by various researchers toward modeling of loop heat pipes and capillary pumped loops. In one approach, the hydrodynamics of flow (i.e. pressure balance) plays the main role and in the other approach the energy balance is taken as the main tool to analyze the system. In the present work, a non-adiabatic closed loop heat transport device has been studied by a combination of the aforementioned methods, i.e. both momentum and energy equations. This work has attempted to improve the available models for the performance analysis of a micro loop heat pipe. To the authors’ knowledge, none of the prior models predict the temperature distribution at the surface of the heat pipe. Incidentally, this surface temperature is one of the most important design parameters and should not exceed a certain temperature during the normal operation of the device.

This work is the continuation of a previous simulation attempt [1] for a similar design. The advantage of this specific design lies in important factors such as simplicity of design, ease of microfabrication and the capability to be simultaneously fabricated as an integrated cooling system along with an electronic device that requires cooling. In this work, the steady-state temperature at the surface of the heat source is predicted. Additionally, the effect of the grooves extension into evaporator is considered in this model.

Principles and analysis

A schematic diagram of a micro loop heat pipe (MLHP) is illustrated in figure 1. It consists of an evaporator–CC assembly, a condenser and liquid and vapor lines. The wicking

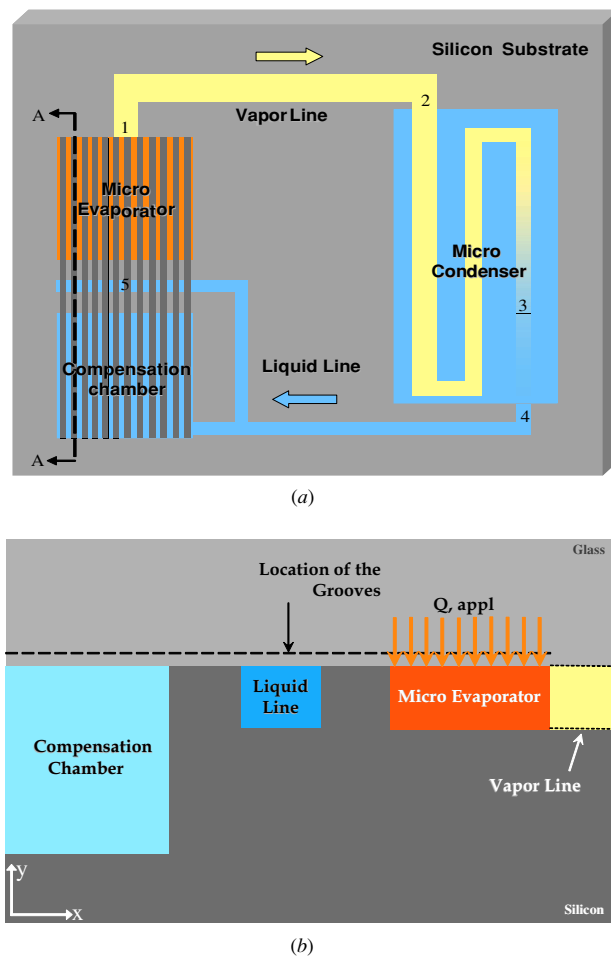


Figure 1. A schematic of the micro loop heat pipe: (a) the overall loop; (b) the cross section A–A shown in (a).

structure is an array of micro-grooves with a rectangular cross-section etched in a silicon wafer. Application of heat to the evaporator surface causes the liquid to vaporize. Subsequently, the pressure build-up due to the process of evaporation forces the vapor to move through the vapor lines into the condenser. Condensation in the condenser discharges the heat absorbed by the liquid in the evaporator and drives the liquid back to the evaporator–CC assembly by the capillary effect of the wicking structure. The pressure generated in the capillary structures is assessed by the law of Laplace for radii of curvature of the menisci in grooves at evaporator-end and at the liquid line-end. The function of CC in the MLHP is to maintain the continuity of the liquid flow and delay dry-out to higher heat inputs.

Similar to our previous work [1], the temperature of the grooves in the evaporator-end was related to that of liquid line-end through the following relation [10–13]:

$$T_e - T_{ll} = \left(\frac{dT}{dP} \right)_{\text{sat}} \Delta P_{\text{Ext}} \quad (1)$$

where ΔP_{Ext} is the total pressure drop in the loop subtracted by the pressure drop in the wicking structure, ΔP_g , hence causing the temperature difference between the evaporator and compensation chamber independent of the geometry or characteristics of the wicking structure. Note that two distinct phenomena are involved in the capillary wicking structure: the

skin friction due to flow of fluid in the grooves, and pumping due to the capillary pressure generation. The net pumping pressure generation is obtained by subtracting the friction pressure loss from the total capillary pressure generated. On the other hand, at the steady state, we must have

$$\Delta P_{15} = P_5 - P_1 = \Delta P_{\text{cap}} - \Delta P_g \quad (2)$$

$$\Delta P_{\text{cap}} = \Delta P_{\text{tot}}. \quad (3)$$

Only one more assumption is needed to arrive at equation (1) and that is to assume all points on the wicking structure are at saturation conditions.

There are two main issues with this type of analysis. One, based on the arguments following equation (1), a model constructed on this basis [11, 12] will be sensitive to the characteristics and configurations of the wicking structure only through the effective wick conductivity. It implies that two completely different wicking structures could bring about similar results if the wick effective conductivities were equal, regardless of how different hydrodynamic effects are in the wicking structures. This issue becomes even more important in MLHP where the wicking structure, or grooves, occupies only a small fraction of the heat passage cross-section area from the evaporator to the liquid line, hence making the effective conductivity practically independent of the characteristics and configuration of grooves structure. Therefore, the model built upon this assumption will be essentially insensitive to the wicking structure's characteristics. To the knowledge of the authors, this issue has not so far been addressed. The grooves in the device under investigation are extended to the evaporator with no change in geometry or cross-section dimensions, therefore allowing some grooves-characteristics dependence for overall device performance.

The second issue is that the assumption of saturation condition in the wicking structure, by which equation (1) is derived, is not valid in all situations. For example for very high heat fluxes, this condition is not physically satisfied but the model still predicts a heat removal capability. To cope with this problem, a capillary limit analysis is also performed in parallel and a maximum heat removal capability based on the capillary limit is evaluated. In general, parallel analyses based on equation (1) are performed by a) optimizing the geometry and dimensions of the grooves and b) assuring a steady-state condition.

The new model was constructed on the previous model in order to include more influential physical factors such as ambient temperature and heat transfer coefficients in different sections of the MLHP. Also, the amount of mass flow rate and heat absorbed by the evaporator, as well as evaporator's temperature were calculated by the computational fluid dynamics (CFD) routine instead of analytical methods which was the case in the previous model. The present model is different from its previous version essentially in the following aspects:

- Operating and evaporator surface temperatures are calculated as functions of the applied heat, and not vice versa which was the case in the previous model.
- The 2D CFD conduction model results determine and update most of the key quantities used in the model such as \dot{m} , \dot{Q}_{ev} , T_{ev} , $T_{\text{ev,surf}}$, etc.

- Due to difficulties introduced by various boundary conditions existing in the CFD model, an ADI (alternate direction implicit) scheme was used which is unconditionally stable.
- As in the previous version, the heat leak must be absorbed in the subcooling section of the condenser. In this model, this energy balance is checked through the evaluation of T_{sc} , T_{ll} and T_{e} instead of calculating the heat leak.

As was mentioned before, in terms of the results, the most important improvement which was the main objective for developing this newer version was to establish the capability of predicting the temperature distribution at the surface of the heat source.

Model description

The CFD model uses the ADI scheme to solve the domain shown in figure 1(b). The governing equation and the boundary conditions are as follows:

$$\nabla^2 T = 0 \quad (4)$$

$$T = T_{\text{ll}} \quad \text{at liquid line surface} \quad (5)$$

$$k \frac{\partial T}{\partial n} = h_{\infty}(T_{\infty} - T) \quad \text{for ambient} \quad (6)$$

$$k \frac{\partial T}{\partial n} = h_{\text{e}}(T_{\text{sat}} - T) \quad \text{for evaporator} \quad (7)$$

$$k \frac{\partial T}{\partial y} = \frac{Q_{\text{appl}}}{A_{\text{e}}} \quad \text{for the heat input site.} \quad (8)$$

The value for T_{ll} is determined by knowing the T_{sink} as an input and a lump-sum analysis for the heat transfer in the liquid line:

$$\dot{m}C \frac{dT}{d\xi} = -h_{\infty} P_{\text{ll}}(T - T_{\text{amb}}). \quad (9)$$

where P_{ll} is the perimeter of the liquid line and ξ is the coordinate in the direction of the liquid line toward the CC. This equation is solved with the boundary condition:

$$T = T_{\text{sc}} \quad \text{at} \quad \xi = 0. \quad (10)$$

The liquid temperature drops very rapidly in the subcooling section of the condenser and approaches T_{sink} due to the fact that the channel depths are very small. Typical values for heat transfer coefficients were used. For the evaporating surface in the evaporator, data of [14] were used and the dependence of results on this value was investigated. These findings are presented in the results section. For single phase liquid flow in the subcooling section of the condenser, the boundary layer correlations for constant wall temperature were used ($Nu = 2.98$) as in [11, 12] and finally typical natural convection heat transfer coefficients were used for interaction with ambient and the evaporator's bottom and sidewall ($h \approx 10 \text{ W m}^{-2} \text{ K}^{-1}$).

Pressure drops in the vapor and liquid lines and the evaporator were calculated using the correlation for rectangular channels [15]:

$$\Delta P = \frac{\rho \bar{V}^2 f L}{2 D_h} \quad f \text{Re}_h = \frac{64}{\frac{2}{3} + \frac{11}{24} \frac{h}{w} \left(2 - \frac{h}{w}\right)} \quad (11)$$

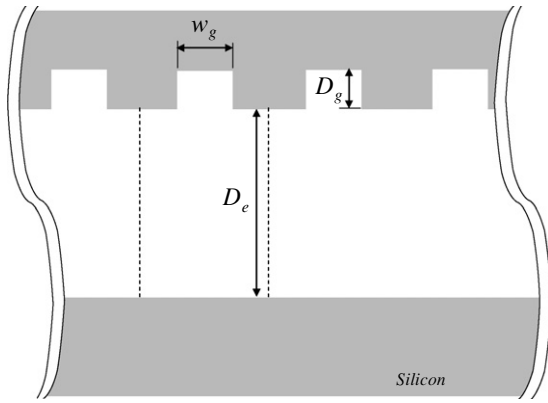


Figure 2. A schematic of the flow cross-section in the evaporator section.

while the pressure drop inside the grooves is calculated by the following equation [16] where α^* is the channel's aspect ratio, width/depth ($0 \leq \alpha^* \leq 1$):

$$f Re_h = 96(1 - 1.3553\alpha^{*2} + 1.9467\alpha^{*4} - 1.7012\alpha^{*6} + 0.9564\alpha^{*8} - 0.2537\alpha^{*10}). \quad (12)$$

The pressure drop in the condenser was treated as before [1], using the methodology of [17] or [11, 12], and recently [3].

The pressure drop in the evaporator was calculated as follows. The cross-section of the evaporator (the flow area) under analysis is shown in figure 2. The flow was assumed to be vapor. This assumption is supported by the fact that the thin liquid film thickness occupies a very small portion of the evaporator's cavity. The hydraulic diameter of the evaporator was defined and calculated as follows:

$$D_{he} = 2 \frac{D_v W_e + N_g D_g W_g}{D_v + W_e + N_g D_g}. \quad (13)$$

The corresponding pressure drop was calculated by correlations given by (11).

Compensation-chamber sizing and fluid inventory calculations

Following the same procedures described in [1], the amount of the working fluid charge, and subsequently, the volume of the compensation chamber were calculated as

$$M_{cold} = \rho_{l,c} V_{tot} + \rho_{l,c} V_{cc} \beta + \rho_{v,c} V_{cc} (1 - \beta) \quad (14)$$

$$M_{hot} = \rho_{v,h} (V_{tot} - V_g) + \rho_{l,h} V_g + \rho_{l,h} V_{cc} (1 - \alpha) + \rho_{v,h} V_{cc} \alpha \quad (15)$$

where $\beta = V_{l,cc}/V_{cc}$ in the cold base and V_{tot} is the total volume of the loop cavity excluding the CC, while $\alpha = V_{l,cc}/V_{cc}$ in the hot base. Also the arranged space in the CC should be adequate. For instance [13]

$$M \leq \rho_{l,max} V_{tot}. \quad (16)$$

Hence the CC volume can be calculated. It should be noted that the simulation results were obtained for the most favorable situation of minimum possible charging as described in [1]. Figure 3 shows the components of the device including the compensation chamber drawn to scale.

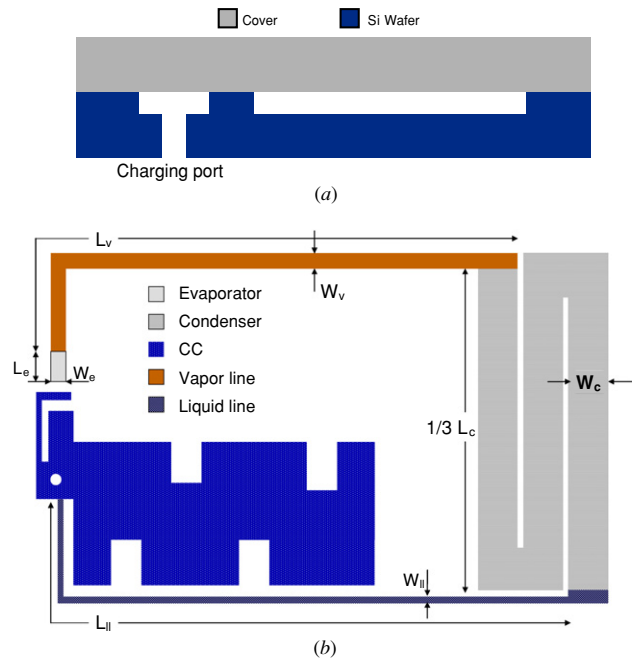


Figure 3. A layout of the micro loop heat pipe: (a) side view of MLHP; (b) the overall loop sketched to scale. The compensation chamber's support columns are designed to provide adequate structural strength.

Solution method

The flowchart of the algorithm is given in figure 4. The purpose of this code is to find the corresponding evaporator surface temperature for a given heat input, Q_{appl} . In order to determine the evaporator temperature, the code was developed such that for any given value of T_{sat} , a quantity called 'error' was calculated. This quantity is explained in the next paragraph. In order to arrive at a solution for T_{sat} , the error must be minimized. This was done using a simple interpolative/extrapolative bi-section method, and the convergence criterion was met once the 'error' fell below a certain small predetermined value. For the reasons mentioned in the following paragraphs, 'error' was assumed a monotonic function of T_{sat} ; therefore the bi-section method would find the only existing solution.

As seen in the flowchart, for every value of T_{sat} , the CFD model is able to calculate the mass flow rate and, consequently, the component pressure drops can be evaluated. Next, equation (1) was used to relate the total external pressure to the temperature difference between the liquid line and the evaporator. Knowing the liquid line temperature, the evaporator's temperature is found semi-analytically. On the other hand, the evaporator's temperature is known directly from the solution of the CFD model. In the steady-state condition, these two values for T_{ev} should be equal. Therefore by naming 'error', the norm of the difference between two calculated values for T_{ev} , we can define a convergence criterion. The saturation temperature–pressure data were acquired from Engineering Equation Solver (EES) software [18] and curve fitted by a nonlinear least-square curve fitting tool of MATLAB on a polynomial function.

The monotonicity of 'error' becomes apparent by analyzing how this function is calculated. The CFD model

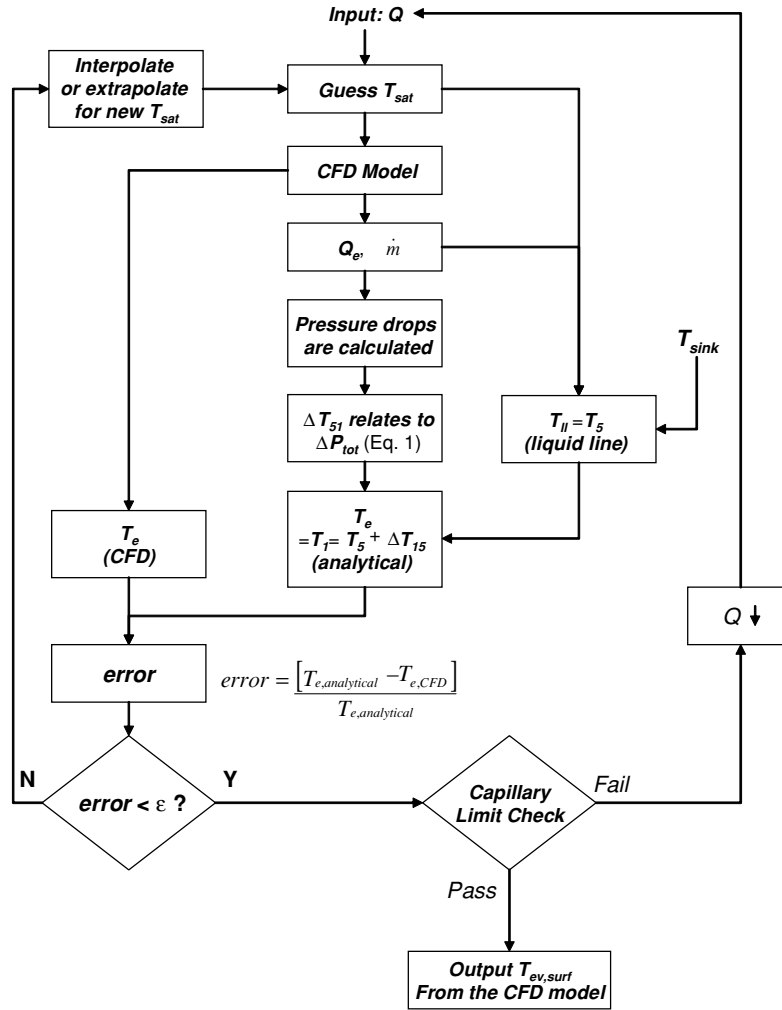


Figure 4. A flowchart of the numerical solution algorithm.

provides higher values for T_{ev} as Q_{appl} increases since the temperature inside the domain is expected to increase for a given T_{sat} . In addition, the vapor pressure curve is monotonous and almost exponential (e.g., the Clasius–Clapeyron equation) therefore the quantity factoring the ΔP_{Ext} in (1) is also exponential and monotonous. As a result, because T_{ev} and $T_{sat,CFD}$ are both monotonous with respect to T_{sat} , their difference, ‘error’, is also monotonous, therefore, the problem has only one solution if any.

This method, as explained previously [1], relies on the assumption that the loop is capable of continuing its operation for any Q_{appl} and T_{sat} . This is obviously incorrect because the maximum pressure generation in the capillary structures (wick) is limited and mainly depends on the geometry, and choice of material. For this reason, after the code converges, the resultant pressure drops are compared with the maximum possible pressure generation in the grooves for a contact angle of zero:

$$\Delta P_{cap} = \Delta P_{cap,max} = 2\sigma/R. \quad (17)$$

Here R is taken as

$$R = D_h/2 \quad (18)$$

where D_h is the hydraulic diameter of the grooves. If there is a pressure deficit, the loop is unable to handle the input heat, and therefore the procedure must be repeated for a smaller Q_{appl} .

Results and discussion

The results of this work are presented and briefly discussed in this section. Figures 5 and 6 demonstrate typical temperature distribution results. Figure 5 shows the 2D temperature field in the cross section of the evaporator–CC assembly corresponding to figure 1(b). As expected the maximum temperature occurs in the region where Q_{appl} is applied. Figure 6 shows the temperature distribution along the evaporator’s top surface. The surface temperature of the CC is nearly equal to the ambient temperature. The minimum temperature occurs around $x = 4.5$ mm which corresponds to the liquid line temperature. The maximum temperature occurs approximately at the center of the evaporator top surface where the heat is applied.

A comparison between the current modeling results and those of [1] is performed and shown in figure 7. It should be noted that the results of each model correspond to their optimized geometries, which are slightly different. However, as seen in figure 7, the trends of the results for both models are

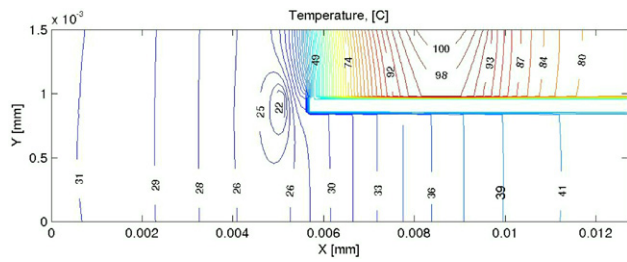


Figure 5. A typical temperature distribution in the evaporator-CC cross section.



Figure 6. A typical temperature profile along the evaporator-CC's top surface.

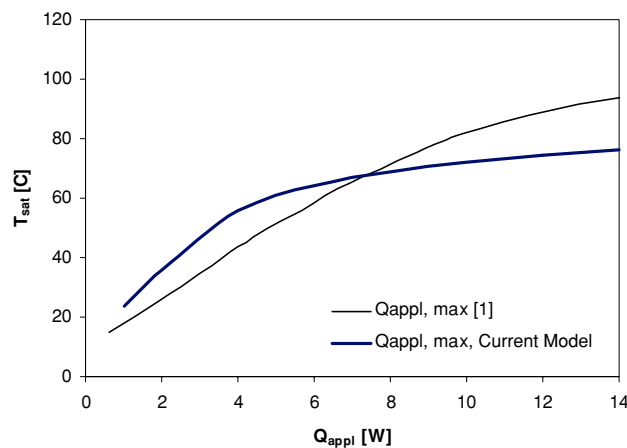


Figure 7. A comparison between the current model and [1].

similar for the range of parameters of interest. In addition, the previous model [1] was validated by performing simulations for a macro scale case for which experimental data existed [1]. A typical behavior of T_{surf} versus Q_{appl} is shown in figure 8. The results indicate that the surface temperature increases with increasing the applied heat. Figure 8 also presents the two-phase length of the condenser. This calculation is necessary to ensure that the two-phase length of the condenser remains less than the total condenser length under all working conditions.

The dimensions of the grooves can be optimized for highest heat transport, but this optimum geometry which is

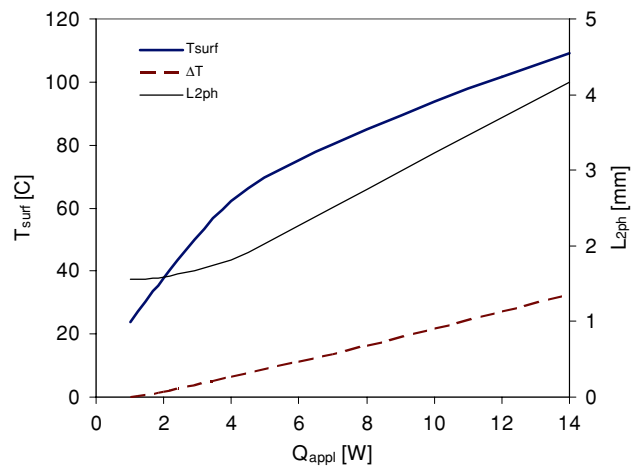


Figure 8. Maximum evaporator outside temperature and the two-phase length of the condenser as functions of the heat input.

Table 1. A partially optimized geometry of the MLHP.

Width of the grooves, W_g	7 μm
Width of the grooves' walls, W_w	2 μm
Length of the grooves, L_g	500 μm
Depth of the grooves, D_g	15 μm
Length of the vapor line, L_v	20 mm
Length of the liquid line, L_{ll}	30 mm
Width of the vapor line, W_v	2 mm
Width of the evaporator, W_e	2 mm
Depth of the microfabricated silicon wafer, D	150 μm
Length of the condenser, L_c	10 mm

based on maximum heat transport capability is not necessarily the most favorable operating condition. Therefore, two distinct aspects of optimization exist here depending on whether a maximum allowable temperature is critical or a better heat removal capability; or a combination of both. The temperature control is especially important in the case of temperature-sensitive electronic devices. The geometry dimensions were partially optimized for maximum heat transport capability and the optimized dimensions are presented in table 1.

Figures 9–12 show the effects of groove geometry on the maximum surface temperature and heat removal. As clearly seen from these figures as well as from our previously reported results [1], the device demonstrates a higher heat transport capability for a lower width of groove walls or groove length (in the wicking structure). Also, these results indicate that there is an optimum groove depth and groove width for which the heat removal capability is maximum. The optimum dimensions correspond to an aspect ratio of 0.5 for the grooves. The reason such optimum dimensions exist is that there is always a trade-off between the effects of two phenomena: the capillary pressure generation and the grooves' pressure drop. That is, on one hand, the capillary pressure generation increases by refining the groove geometry, but on the other hand, the pressure loss also increases due to a smaller flow passage area. Figures 13–15 depict the effect of other geometry parameters, namely vapor line width, evaporator's width and the depth of etched structures, respectively. As can be seen in these figures, the device demonstrates a better performance for a wider vapor line, a wider evaporator and deeper etched structures.

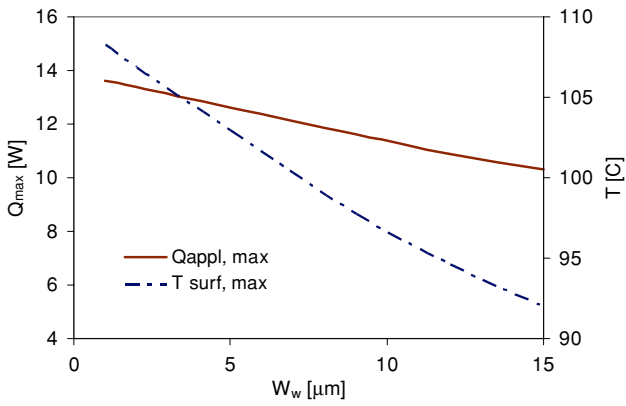


Figure 9. Effect of grooves' wall thickness on the performance.

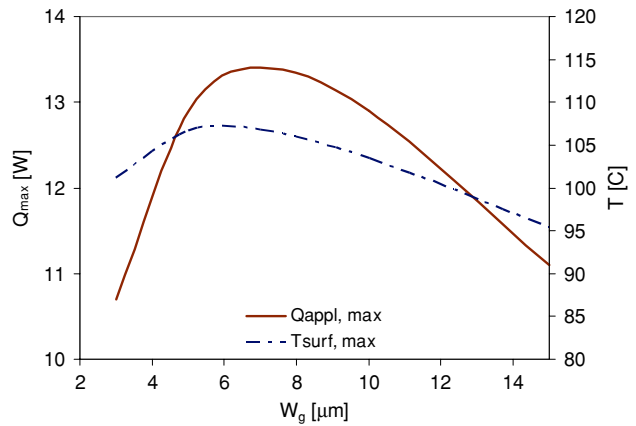


Figure 12. Effect of grooves' width on the MLHP performance.

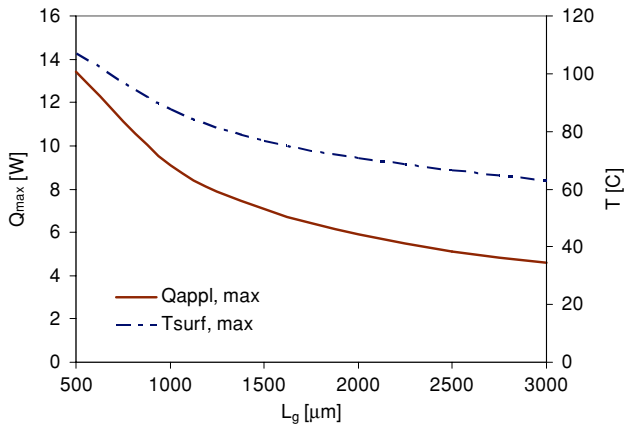


Figure 10. Effect of grooves' length on the MLHP performance.

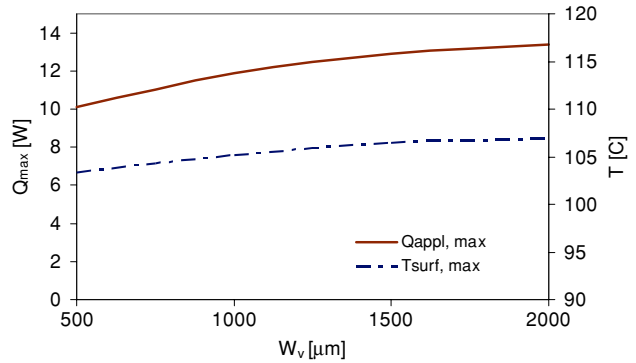


Figure 13. Effect of vapor line's width on the MLHP performance.

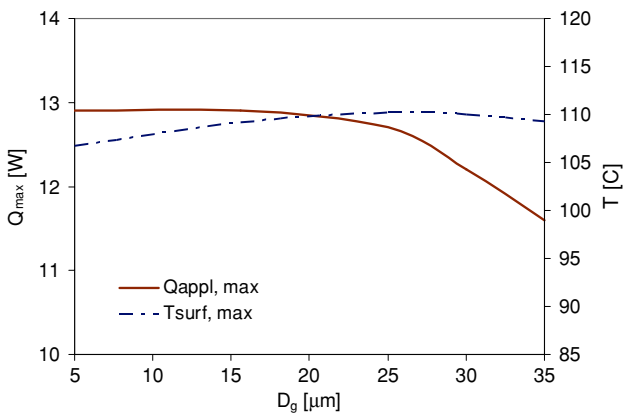


Figure 11. Effect of grooves' depth on the MLHP performance.

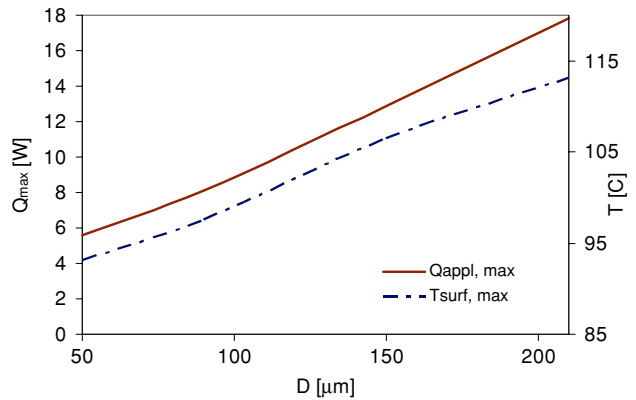


Figure 14. Effect of the depth of etched structures on performance.

Figure 16 studies the effect of the heat transfer coefficient on the surface temperature. As seen in this figure, the surface temperature decreases with increasing the heat transfer coefficient. However, the surface temperature becomes less sensitive to the heat transfer coefficients at higher heat transfer coefficients (in the range of $30\,000\text{ W m}^{-2}\text{ K}^{-1}$ or higher). This could be explained as follows. As the heat transfer coefficient increases, the mass flow rate increases, resulting in a higher total pressure drop. This causes the model to predict a higher operating temperature (see equation (1)). This effect partially offsets the effect of a higher heat transfer coefficient that naturally leads to a lower temperature.

All results are obtained for water as the working fluid, a heat sink surface temperature of $10\text{ }^{\circ}\text{C}$ and an ambient temperature of $20\text{ }^{\circ}\text{C}$. Figure 17 shows the dependence of results on T_{amb} . The results show that the effect of the ambient temperature on the performance is more pronounced at lower heat loads. However, this effect becomes less important as the heat input exceeds approximately 5 W . The effect of the sink temperature in these simulations turned out to be negligible. A lower sink temperature yields a lower condenser exit (subcooled liquid) temperature. This, in general, should cause the temperature of the liquid entering the evaporator-CC to drop and therefore, improve the performance of the device

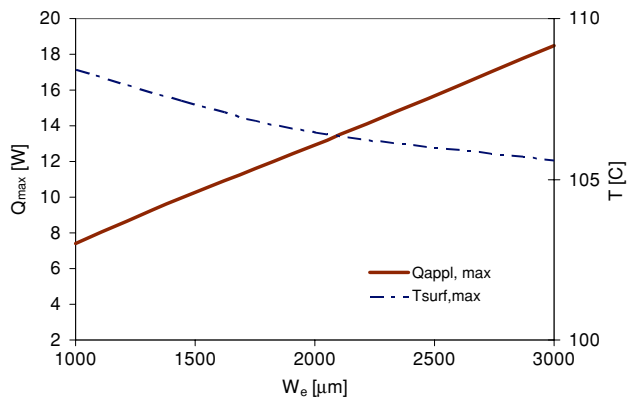


Figure 15. Effect of evaporator’s width on performance.

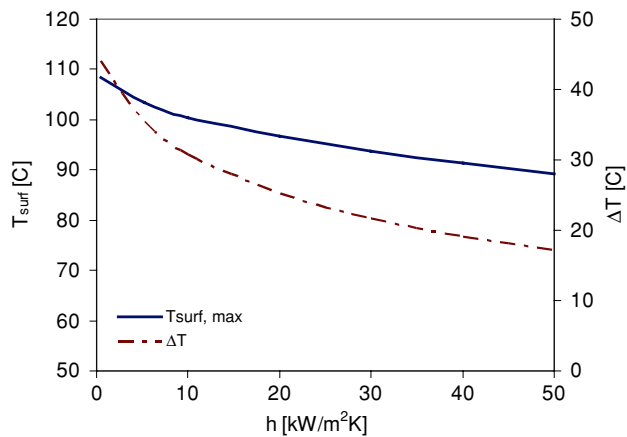


Figure 16. The surface temperature as a function of the heat transfer coefficient for a heat load of 10 W. ($\Delta T = T_{surf,max} - T_{sat}$).

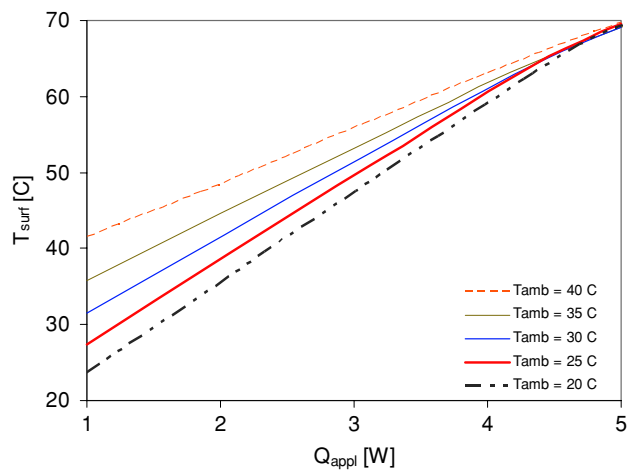


Figure 17. Effect of the ambient temperature on device performance.

by lowering the evaporator’s temperature. However, as the device is miniaturized, the ambient has the ultimate effect and the liquid temperature approaches the ambient temperature very rapidly hence diminishing the effect of a lower sink temperature.

These simulation results indicate that the vapor temperature in the evaporator, T_{sat} , increases monotonously

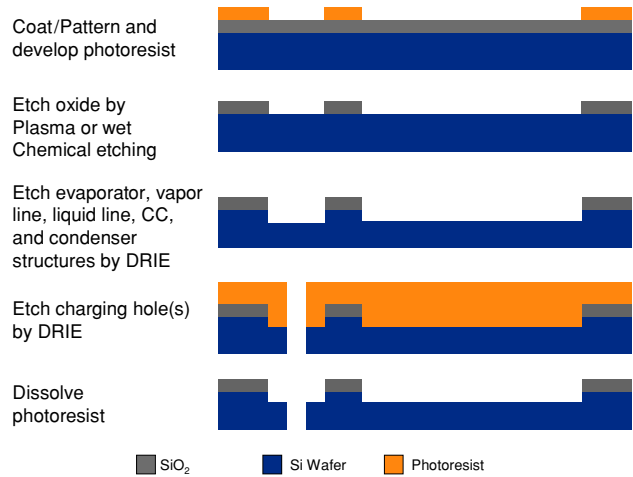


Figure 18. A simplified microfabrication process for the silicon wafer.

with Q_{appl} . However, if we decrease the length of the liquid line by an order of magnitude, there will be a minimum in the $Q_{appl}-T_{sat}$ curve as has been reported previously [13]. This is because of the non-adiabatic liquid line boundary condition and the effect of a high ambient temperature on elevating the liquid temperature before entering the evaporator–CC assembly. Incidentally, this is also the cause for the model to be indifferent to a sink temperature: the liquid is practically at T_{amb} when entering the evaporator–CC assembly. A variation in T_{sink} , however, changes the two-phase length of the condenser which in turn has implications on the condenser pressure drop and consequently on the performance, although negligible.

Microfabrication

The microfabrication steps for the micro loop heat pipe are illustrated in figure 18. In order to allow flow visualizations during operation, a glass wafer is used to cap the MLHP. In this work, the wicking structures are fabricated in the glass substrate. The micro evaporator, micro condenser, compensation chamber and liquid and vapor lines are etched into a silicon wafer. Temperature distributions along the MLHP are measured using integrated micro RTD sensors. The micro heater and micro RTDs are fabricated by a standard lift-off process. Holes will be drilled through the glass wafer to facilitate charging of the MLHP with the working fluid. A tube will be connected to the backside of the glass wafer via a through hole to serve as the CC feed line.

Conclusion

A newer version of the model developed for a MLHP [1] was presented. This version of the code is capable of predicting the evaporator’s surface temperature as a function of heat input, ambient temperature and geometry. This is especially important because in the application of interest, the heat source is usually a very temperature-sensitive electronic component that must be cooled and maintained below a certain temperature. The optimized dimensions were found to be a groove wall thickness of $2 \mu m$, a groove width of $7 \mu m$, a

wicking structure length of 500 μm and a vapor line width of 2 mm. It was observed that a theoretical heat removal of up to 150 W cm^{-2} at a maximum surface temperature of 100 $^{\circ}\text{C}$ is possible by making use of this device.

Acknowledgments

This work was partially supported by a grant from the South Carolina Space Grant Consortium.

References

- [1] Ghajar M, Darabi J and Crews N Jr 2005 A hybrid CFD-mathematical model for simulation of a MEMS loop heat pipe for electronics cooling applications *J. Micromech. Microeng.* **15** 313–21
- [2] Gerasimov Y and Maidanik Y F 1974 Heat Pipe *USSR Inventors Certificate* 449213
- [3] Hoang T T and Ku J 2003 Heat and mass transfer in loop heat pipes *Proc. HT2003, # HT2003-47366 ASME Summer Heat Transfer Conf. (Las Vegas, NV, USA, 21–23 July)*
- [4] Hoelke A, Henderson H T, Gerner F M and Kazmierczak M 1999 Analysis of the heat transfer capacity of a micromachined loop heat pipe *Proc. ASME HTD-vol 364–3* ed L C White pp 53–60
- [5] Mantravadi N 2000 MEMS-based development of a silicon CPS wick for loop heat pipe applications *Master's Thesis* University of Cincinnati, Cincinnati, OH
- [6] Hamdan M O 2003 Loop heat pipe (LHP) modeling and development by utilizing coherent porous (CPS) wicks *PhD Dissertation* University of Cincinnati, Cincinnati, OH
- [7] Muraoka I, Ramos F M and Vlasso V V 2001 Analysis of the operational characteristics and limits of a loop heat pipe with porous element in the condenser *Int. J. Heat Mass Transfer* **44** 2287–97
- [8] Pastukhov V G, Maidanik Yu F, Vershinin C V and Korukov M A 2003 Miniature loop heat pipes for electronics cooling *Appl. Therm. Eng.* **23** 1125–35
- [9] Kaya T and Ku J 2003 Thermal operational characteristics of a small-loop heat pipe *J. Thermophys. Heat Transfer* **17** 464–70
- [10] Maydanik Yu F 2005 Loop heat pipes (review) *Appl. Therm. Eng.* **25** 635–57
- [11] Kaya T and Hoang T 1999 Mathematical modeling of loop heat pipes *AIAA Paper* 99-0477
- [12] Hoang T and Kaya T 1999 Mathematical modeling of loop heat pipes with two-phase pressure drop *AIAA Paper* 99-3448
- [13] Ku J 1999 Operating characteristics of loop heat pipes *SAE Technical Paper* 1999-01-2007
- [14] Izenson M G and Crowley C J 1992 Design of condensing radiators for spacecraft thermal management *AIAA Paper* A92-47847
- [15] Khrustalev D and Faghri A 1995 Heat transfer during evaporation on capillary grooved structures of heat pipes *J. Heat Transfer* **117** 740–7
- [16] Blevins R D 1984 *Applied Fluid Dynamics Handbook* (New York: Van Nostrand Reinhold)
- [17] Shah R K and Bhatti M K 1987 Laminar convective heat transfer in ducts *Handbook of Single Phase Convective Heat Transfer* ed S Kacac, R K Shah and W Aung (New York: Wiley)
- [18] Izenson M G and Crowley C J 1992 Design of condensing radiators for spacecraft thermal management *AIAA Paper* A92-47847
- [19] Klein S A 2004 Engineering Equation Solver version 7.171, Educational version distributed by McGraw Hill